

Accounting for localized deformation: a simple computation of true stress in micropillar compression experiments

Jalal Smiri^{1†}, Oğuz Umut Salman^{1†}, Matteo Ghidelli^{1†},
Ioan R. Ionescu^{1,2*†}

¹*LSPM, University Sorbonne Paris Nord, av. J.P Clement,
Villetaneuse, 93430, France.

²IMAR, Romanian Academy, str. Grivitei, Bucharest, 10587, Romania.

*Corresponding author(s). E-mail(s): ioan.r.ionescu@gmail.com;
Contributing authors: jalal.smiri@edu.sorbonne-paris-nord.fr;
oguzumut.salman@cnrs.fr; matteo.ghidelli@lspm.cnrs.fr;

†These authors contributed equally to this work.

Abstract

Background: Compression experiments are widely used to study the mechanical properties of materials at micro- and nanoscale. However, the conventional engineering stress measurement method used in these experiments neglects to account for the alterations in the material's shape during loading. This can lead to inaccurate stress values and potentially misleading conclusions about the material's mechanical behavior, especially in the case of localized deformation.

Objective: Our goal is to calculate true stress in cases of localized plastic deformation from standard experimental data (displacement-force curve, aspect ratio, shear band angle and elastic strain limit).

Methods: We use a simple mechanical-geometrical approach based on reasonable physical assumptions to get analytic formulas of true stress and eliminating the need for finite element computations. Furthermore, in numerical simulations of pillar compression, the formula-based true stress demonstrates strong alignment with the theoretical true stress.

Results : We propose analytic formulas for calculating true stress in cases of localized plastic deformation commonly encountered in experimental settings for a single band oriented in arbitrary directions with respect to the vertical axis of the pillar.

Conclusions : The true stress computed with the proposed formulas provides a more precise interpretation of experimental results and can serve as a valuable and simple tool in material design and characterization.

Keywords: micro-pillars, compression experiments, shear bands, true stress

1 Introduction

Compression experiments conducted on pillars have proven to be a valuable method for analyzing the mechanical behavior of materials at the micro- and nano-scales. This approach involves the fabrication of micro-pillars (often with focused ion beam (FIB) techniques) followed by an uni-axial compression to study its mechanical response in a deformation process under displacement or load control. This method has been particularly useful for investigating the onset and evolution of plastic deformation in materials, by exploring the local deformation mechanism (when compression test are carried out in situ SEM), see for instance [Uchic et al \(2004\)](#); [Greer et al \(2005\)](#); [Ng and Ngan \(2008\)](#); [Frick et al \(2008\)](#); [Kiener et al \(2011\)](#); [Friedman et al \(2012\)](#); [Zhang et al \(2017b\)](#); [Salman and Ionescu \(2021\)](#); [Zhang et al \(2020\)](#); [Salman et al \(2021\)](#); [Cui et al \(2021\)](#). Specifically, micro-pillar compression experiments have revealed numerous new phenomena, including the transition from wild-to-mild plasticity [Zhang et al \(2017b\)](#), pristine-to-pristine plastic deformation [Wang et al \(2012\)](#), the "smaller is stronger" effect [Lee et al \(2009\)](#), size- and shape-dependent flow stresses [Uchic et al \(2004\)](#); [Maaß et al \(2012\)](#); [Zhang et al \(2017a\)](#) and, microstructural control of plastic flow [Rizzardi et al \(2022\)](#), among others.

During such compression experiments, the material can undergo significant plastic deformation, which can manifest in either homogeneous deformation or slip/kink bands [Hagihara et al \(2016\)](#); [Mayer et al \(2016\)](#); [Basak et al \(2019\)](#); [Chen et al \(2020\)](#); [Nandam et al \(2021\)](#); [Weiss et al \(2021\)](#); [Nizolek et al \(2021\)](#); [Marano et al \(2021\)](#); [Zhang et al \(2022\)](#). Homogeneous deformation occurs when the material undergoes uniform deformation throughout its structure, while slip/kink bands result from localized deformation that can form along some preferred orientation [Inamura \(2019\)](#); [Gan et al \(2020\)](#). The resulting engineering strain-stress curve is related to a displacement-force experimental recording, but in order to accurately characterize the material's mechanical behavior, it is necessary to determine the Eulerian (true) stress that is exerted within the deformation zone. It is especially crucial to be able to accurately interpret the mechanical properties of engineered or designed materials using various methods to assess whether desired enhancements have been achieved [Wu et al \(2021\)](#); [Ghidelli et al \(2021\)](#). The significance of using true stress in assessing mechanical responses has been discussed in prior studies related to the mechanical behavior of metallic glass [Han et al \(2008\)](#); [Wang et al \(2017\)](#). However, of particular importance is the fact that, to the best of our knowledge, there is currently no established method to calculate the required load-bearing area to evaluate true stress, during plastic localization mechanisms.

In this context, the aim of this study is to derive simple formulas for calculating true stress in cases involving slip/kink band formation during mechanical loading while avoiding the need for lengthy and complex finite element computations that deal with large deformations of crystals. Specifically, we consider a localization, observed frequently in experiments as single band oriented in arbitrary directions with respect to the vertical axis of the pillar, for which we derive a formula and employ it to assess the reliability of previous experimental results. We have to mention here that the proposed formula is completely geometric. Contrary to Finite Elements (FE) computations, it does not need any material modeling setup, hence it could be very useful in choice of the constitutive law.

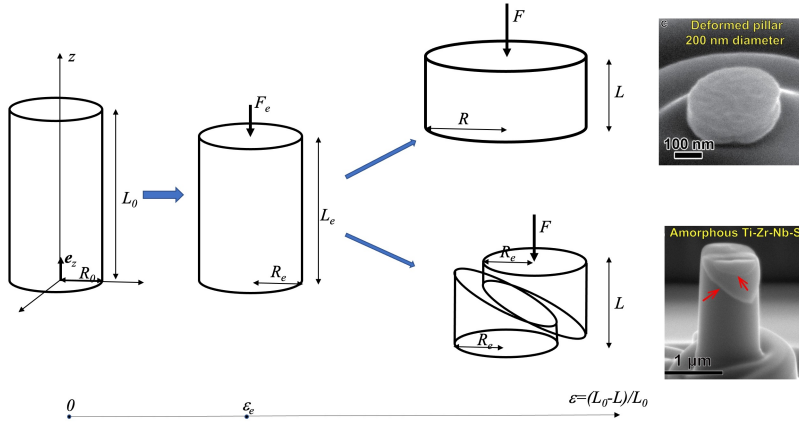


Fig. 1 Schematic representation of the nano or micro-pillar deformation. The linear elastic regime, $\epsilon^{eng} < \epsilon_e$, is followed by one of the two types of plastic flow. Up: homogeneous deformation, Bottom: shear/kick band deformation (experimental illustration taken from [Wu et al \(2021\)](#)).

2 Simple modeling of pillars' deformation

After the initial loading process, which is associated with small-strain linear elastic behavior, the pillars undergo significant plastic deformation, making the elastic deformations negligible in comparison to the plastic ones. From these plastic deformation processes, two distinct scenarios emerge: homogeneous and slip/kink band, as illustrated schematically in Figure 1 and detailed subsequently. The Cauchy stress tensors corresponding to these two deformation mechanisms exhibit different patterns. In either scenario, the primary challenge is to determine the true stress σ^{true} within the uniaxial Cauchy stress tensor $\boldsymbol{\sigma} = -\sigma^{true} \mathbf{e}_z \otimes \mathbf{e}_z$, where \mathbf{e}_i represents the elements of the orthonormal basis of the three-dimensional Euclidean vector space, acting on the active area A_u .

To be more specific, let R_0 and L_0 represent the initial (Lagrangian) radius and height of the cylindrical pillar, respectively, while R and L denote the current (Eulerian) dimensions during deformation, as shown in Fig. 1. Let $\epsilon^{eng} = (L_0 - L)/L_0$ denote the overall engineering strain. Let $\mathbf{F} = -F\mathbf{e}_z$ represent the force applied to the top of the pillar during deformation, where $F = \sigma^{true}A_u$, and let σ^{eng} denote the nominal (engineering) stress, i.e., $F = \sigma^{eng}A_0$, with $A_0 = \pi R_0^2$ is the original cross-sectional area.

We assume knowledge of the initial pillar shape, specifically the aspect ratio $f_0 = L_0/2R_0$, and have access to the engineering strain-stress curve, denoted as the function $\epsilon^{eng} \rightarrow \sigma^{eng}(\epsilon^{eng})$. The primary objective of this paper is to derive a simple formula for estimating the engineering strain-true stress curve, represented as $\epsilon^{eng} \rightarrow \sigma^{true}(\epsilon^{eng})$.

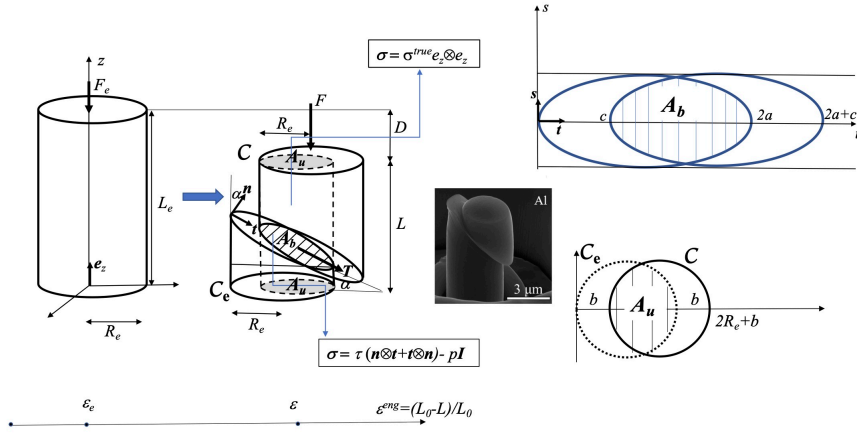


Fig. 2 (Left): Schematic representation of localized plastic deformation following the elastic stage with the Cauchy stress tensor acting in different regions of the pillar. (Right, top): The plan of the shear band with its area A_b between two ellipses representing the upper and lower sections of the pillar. (Right, bottom) : Its projection on the horizontal plane (experimental image taken from Weiss et al (2021)).

2.1 Elastic deformation

For $\epsilon^{eng} < \epsilon_e$ (or equivalently for $\sigma^{eng} < \sigma_e^{eng}$) the pillar exhibits a linear elastic behavior. Here, ϵ_e and $\sigma_e^{eng} = \sigma^{eng}(\epsilon_e)$ represent the strain and stress limits of elasticity, which can be easily identified in each stress-strain (or force-displacement) curve. Since the elastic strain limit ϵ_e , is usually small (less than 3%) the elastic linear theory can be accepted as a good approximation. If the deformed shape is also a cylinder and the stress is uniaxial throughout the pillar then $A_u = A = \pi R^2$, $F = \sigma^{true} \pi R^2$

and $\sigma^{eng} R_0^2 = \sigma^{true} R^2$. For anisotropic materials, such as monocrystals, during the elastic phase, the pillar is no longer a perfect cylinder. However, since the deformation is small, the deviation from a cylindrical shape can be neglected.

Following the Hooke's law the volumetric strain $\epsilon_V = (V_0 - V)/V_0 = (L_0 R_0^2 - LR^2)/L_0 R_0^2 = (1 - (1 - \epsilon^{eng})(R/R_0)^2)$ is related to the true stress through the compressibility modulus K by $\sigma^{true} = 3K\epsilon_V$. We get a second order algebraic equation for $(R_0/R)^2$ to deduce that $(R_0/R)^2 = (1 - \sqrt{1 - 4\delta(1 - \epsilon^{eng})})/2\delta$, where $\delta = \sigma^{eng}/3K$. Finally we have

$$\sigma^{true} = \frac{3K - \sqrt{9K^2 - 12K\sigma^{eng}(1 - \epsilon^{eng})}}{2}, \quad \text{for } \epsilon^{eng} \leq \epsilon_e,$$

which for small values of $\delta_e = \sigma_e^{eng}/3K$ and ϵ_e , gives the well-known formula for true stress:

$$\sigma^{true} = \sigma^{eng}(1 - \epsilon^{eng}), \quad \text{for } \epsilon^{eng} \leq \epsilon_e. \quad (1)$$

Note that since $1 - \epsilon^{eng} \approx 1$ for $\epsilon^{eng} < \epsilon_e$ the difference between the true and engineering stress is not significant, and we can conclude that $\sigma^{true} \approx \sigma^{eng}$ during the elastic phase.

In most strain-stress curves, the elastic strain limit ϵ_e is usually easy to extract by considering the end of the linear behavior. In the following, ϵ_e will be considered as obtained from the experimental results, but this assumption will not imply any further considerations (i.e., ϵ_e) about the hardening or softening plastic behavior of the pillar.

2.2 Homogeneous uni-axial stress

For larger deformations, $\epsilon^{eng} > \epsilon_e$, in the first scenario the deformation is homogeneous and the stress throughout the entire pillar is assumed to be uni-axial, given by $\boldsymbol{\sigma} = -\sigma^{true} \mathbf{e}_z \otimes \mathbf{e}_z$, where $A_u = A = \pi R^2$. For materials modeled by a pressure-independent plasticity law, plastic deformation is isochoric and the volume is preserved. If the deformed shape remains a cylinder and we neglect the further elastic deformation of the volume then we get $V = \pi R^2 L = V_e = \pi R_e^2 L_e$, in which R_e and L_e are, respectively, the radius and length of the pillar at the end of elastic phase (i.e. fixed during post-elastic deformation). After some algebra we find

$$\sigma^{true} = \frac{\sigma_e^{true}}{\sigma_e^{eng}(1 - \epsilon_e)} \sigma^{eng}(1 - \epsilon^{eng}), \quad \text{for } \epsilon^{eng} > \epsilon_e.$$

Since for small values of $\delta_e = \sigma_e^{eng}/3K$ we have $\sigma_e^{true} = \sigma_e^{eng}(1 - \epsilon_e)$ we get the well known formula

$$\sigma^{true} = \sigma^{eng}(1 - \epsilon^{eng}), \quad \text{for } \epsilon^{eng} > \epsilon_e. \quad (2)$$

However, for large values of ϵ^{eng} , using the nominal stress σ^{eng} instead of the Cauchy stress σ^{true} can significantly alter the behavior of the stress-strain diagram, giving a false impression of overall hardening-like behavior.

Due to the boundary conditions on the top and bottom, the above assumption concerning the cylindrical shape of the deformed sample is not always valid. Indeed, barreling or bulging phenomena could occur, and the sample shape is given

by two diameters (the middle one and the top/bottom one). If the minimum between the top/bottom and center radii, denoted by $R_m(\epsilon^{eng})$, could be measured during the experiment, then true stress can be directly computed through $\sigma^{true} = F/(\pi R_m^2(\epsilon^{eng}))$, and we do not need the above formula.

2.3 Slip/kink band plastic deformation

In the second scenario, for $\epsilon^{eng} > \epsilon_e$, deformation is localized in a narrow zone between two parallel planes with a normal vector \mathbf{n} , determined by the angle α with respect to the vertical axis \mathbf{e}_z , see Fig. 2. The Cauchy stress tensor acting in the shear band is given by $\boldsymbol{\sigma} = \tau(\mathbf{n} \otimes \mathbf{t} + \mathbf{t} \otimes \mathbf{n}) - p\mathbf{I}$, where \mathbf{t} is the slip direction, τ is the shear stress and, \mathbf{I} is the identity matrix, while in two cylindrical regions above and below the shear band it is assumed to be uniaxial, i.e., $\boldsymbol{\sigma} = \sigma^{true}\mathbf{e}_z \otimes \mathbf{e}_z$ (see Fig. 2). This assumption is a schematic representation of the stress distribution in the pillar with three non-vanishing uniform stress zones which allows analytic computations. Even if the stress distribution is expected to be much more complicate this assumption seems to be globally verified in FE computations (see for instance Fig 4 bottom).

From the above assumption we can deduce that the expression for shear stress τ , acting in the shear band, is proportional to the true stress:

$$\tau = \frac{1}{2} \sin(2\alpha) \sigma^{true}. \quad (3)$$

It should also be noted that if the true stress σ^{true} is known, then equation (3) enables the calculation of the shear stress τ as a function of the shear plastic strain γ_p , which is proportional to the plastic axial engineering strain and can be expressed as

$$\gamma_p = \frac{L_e - L}{\cos(\alpha)H_b} = \frac{(\epsilon^{eng} - \epsilon_e)L_0}{\cos(\alpha)H_b},$$

in which H_b represents the thickness of the shear band. The diagram of shear stress τ versus shear plastic strain γ_p is a very important tool in any discussion about the choice of the plastic model to be considered, both in crystal plasticity and for amorphous materials.

Let us now compute the area A_u between the two disks (or equivalently $A_b = A_u/\cos(\alpha)$ the area between the two ellipses) \mathcal{C}_e and \mathcal{C} corresponding to the projection on the basal plane of the two cylinders (see Fig. 2). One of the circles is translated by a distance of $b = D \cot(\alpha)$, where $D = L_e - L$ is the vertical displacement of the upper pillar region. After some simple computations, one can find that the area A_u between the two regions is given by

$$A_u = R_e^2 \left[\pi - \frac{b}{R_e} \sqrt{1 - \frac{b^2}{4R_e^2}} - 2 \arcsin \left(\frac{b}{2R_e} \right) \right].$$

Denoting by $f_0 = L_0/2R_0$ the initial shape number and by $f_e = L_e/2R_e = (1-\epsilon_e)^{3/2} f_0$ the shape number at the end of the elastic phase, and by $\epsilon_*^{eng} = (L_e - L)/L_e = (\epsilon^{eng} -$

$\epsilon_e)/(1 - \epsilon_e)$ the engineering (plastic) deformation with respect to the configuration at the end of the elastic phase, we get

$$A_u = R_e^2 \Phi(\epsilon_*^{eng} f_e \cot(\alpha)), \quad (4)$$

where we have denoted by

$$\Phi(s) = \pi - 2s\sqrt{1 - s^2} - 2 \arcsin(s).$$

Taking into account that $R_0^2/R_e^2 = (1 - \sqrt{1 - 4\delta_e(1 - \epsilon_e)})/2\delta_e$ we can deduce that:

$$\sigma^{true} = \frac{\sigma^{eng} \pi (1 - \sqrt{1 - 4\delta_e(1 - \epsilon_e)})}{2\delta_e \Phi((\epsilon^{eng} - \epsilon_e) f_e \cot(\alpha) / (1 - \epsilon_e))}, \quad \text{for } \epsilon^{eng} > \epsilon_e. \quad (5)$$

Bearing in mind that $\epsilon_*^{eng} f_e = (\epsilon^{eng} - \epsilon_e) f_0 \sqrt{1 - \epsilon_e}$ for small values of ϵ_e and δ_e , we have $R_0^2/R_e^2 \approx 1 - \epsilon_e$ we can deduce a simplified formula for the true stress:

$$\sigma^{true} = \frac{\pi(1 - \epsilon_e) \sigma^{eng}}{\Phi((\epsilon^{eng} - \epsilon_e) f_0 \sqrt{1 - \epsilon_e} \cot(\alpha))}, \quad \text{for } \epsilon^{eng} > \epsilon_e \quad (6)$$

Note that to use the simplified formula we only need to know the elastic limit ϵ_e , the shear band angle α and the initial aspect ratio f_0 . However, the exact formula given in Eq. 5 requires also δ_e : the ratio between engineering stress σ_e^{eng} at the end of the elastic phase and the bulk modulus K .

In contrast to the homogeneous deformation scenario, here the true stress is larger than the engineering stress. Therefore, in many strain-stress diagrams, the plateau or softening of the engineering stress should be viewed as a hardening of the true stress.

3 Comparison with 2-D FE computations

In the above model, the shear band thickness is assumed to be small relative to the specimen length (i.e., $H_b/L_0 \ll 1$), a condition verified in many situations. For experiments where this assumption is not verified, Eqs. (5) and (6) need to be revisited. Moreover, due to the Lagrangian description of large plastic deformations in the shear band, finite element simulations must contend with severe distortion of elements. Consequently, their results exhibit a shear band thickness that is unrealistically large, and computations are halted at intermediate strains (less than 20%). Consequently, a conclusive comparison between the above formulas and Lagrangian FE computations could not be made.

For this reason, we will use here an Eulerian approach in the FE computations, capable of describing thin shear bands. We will select an elastic perfectly plastic material (see the Appendix for the constitutive equation) with the Von-Mises yield limit σ_Y , such that the theoretical shear stress in the shear band is known ($\tau_{th} = \sigma_Y/\sqrt{3}$). From Equation (3), we can compute the theoretical true stress $\sigma_{th}^{true} = 2\sigma_Y/(\sqrt{3} \sin(2\alpha))$ for $\epsilon^{eng} > \epsilon_e$. Then, σ_{th}^{true} can be compared with the true stress σ^{true} computed from Equations (5) or (6) and the FE computations of the engineering stress σ^{eng} .

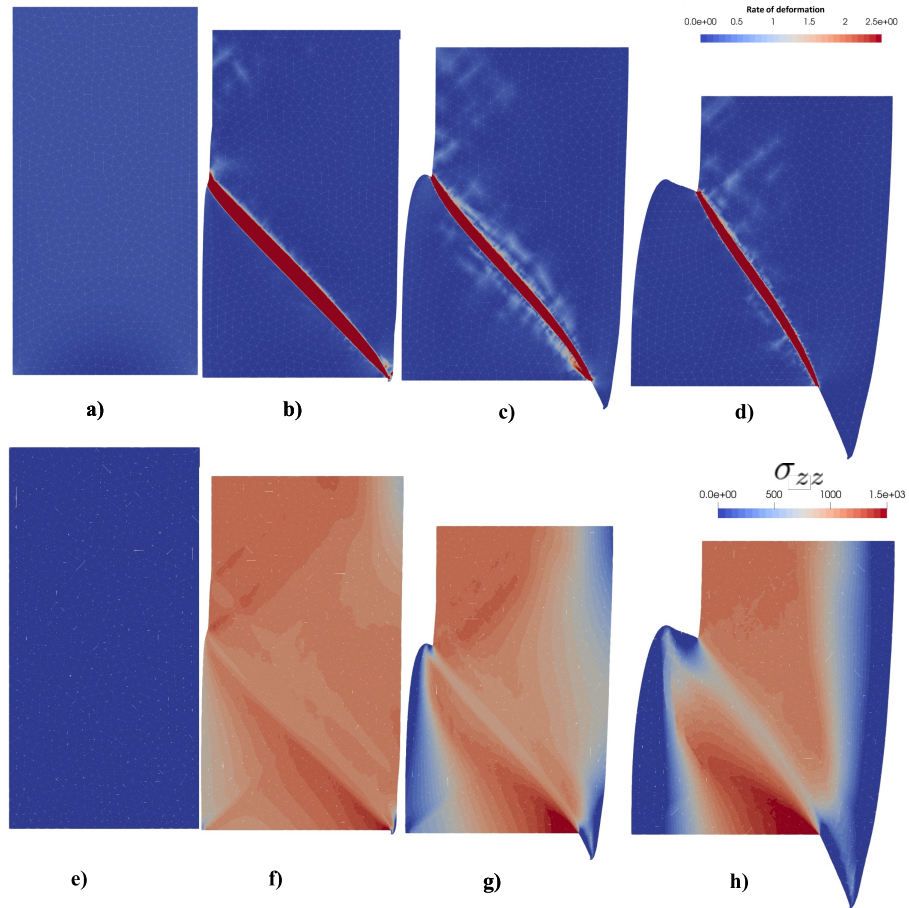


Fig. 3 2D Eulerian FE computation of the shear band localization in an elastic-perfectly plastic pillar with the plastic strain rate $\dot{\epsilon}^p$ (up) and the Cauchy stress σ_{zz} (bottom) in color scale. Evolution from for different values of ϵ^{eng} : 0% in a), 5.5% in b), 11% in c) and 22% in d).

The ALE approaches of the shear bands, which require re-meshing at each time step, are computationally very expensive. Therefore, we have performed only 2-D computations here. For the two-dimensional case, the geometric true stress formula (Equation (6)) reads:

$$\sigma^{true} = \frac{(1 - \epsilon_e)\sigma^{eng}}{1 - (\epsilon^{eng} - \epsilon_e)f_0(1 - \epsilon_e)\cot(\alpha)}, \quad \text{for } \epsilon^{eng} > \epsilon_e. \quad (7)$$

In Figure 3, we have plotted the evolution of the shear band in an elastic-perfectly plastic pillar of initial shape number $f_0 = 2$, with the following material constants: $E = 38235$ MPa, $\nu = 0.34$, $\sigma_Y = 1000$ MPa. We remark that the ALE computations of the Eulerian model were able to handle a thin shear band. The angle of the shear band is, as expected, $\alpha = 45$ at the beginning, but we observe a slight variation at the end of the deformation process. **At the bottom of Fig. 3, the distribution of the Cauchy stress σ_{zz} is plotted. One can remark that this distribution has, globally, a good agreement with the schematic stress distribution plotted in Figure 2.**

In Figure 4, we have plotted the engineering stress σ^{eng} (in orange) computed from the resultant force on the pillar's top of the FE simulations. From this curve, we obtain the elastic strain to be $\epsilon_e = 0.031$. In blue, we have plotted the theoretical true stress σ_{th}^{true} that we expect from the model, and in green, the true stress σ^{true} computed with Equation (7). We observe that the formula-based true stress closely aligns with the theoretical true stress up to $\epsilon^{eng} < 18\%$. After $\epsilon^{eng} = 18\%$, the true stress overestimates the theoretical one. This is due to the variation of the shear band angle α , which is larger at the end of the deformation process.

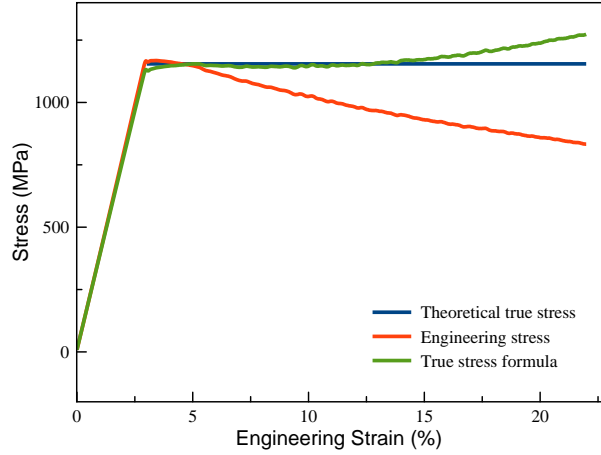


Fig. 4 FE computations with an Eulerian elastic perfectly plastic model of the engineering stress σ^{eng} (in orange). In green the true stress σ^{true} computed with the formula (7) and in blue the theoretical true stress σ_{th}^{true} that we expect from the model.

4 True stress computation and re-interpretation of the stress-strain curves

In this section, we want to illustrate how the formulas deduced in the previous section alter some experimental engineering strain-stress curves reported in the literature.

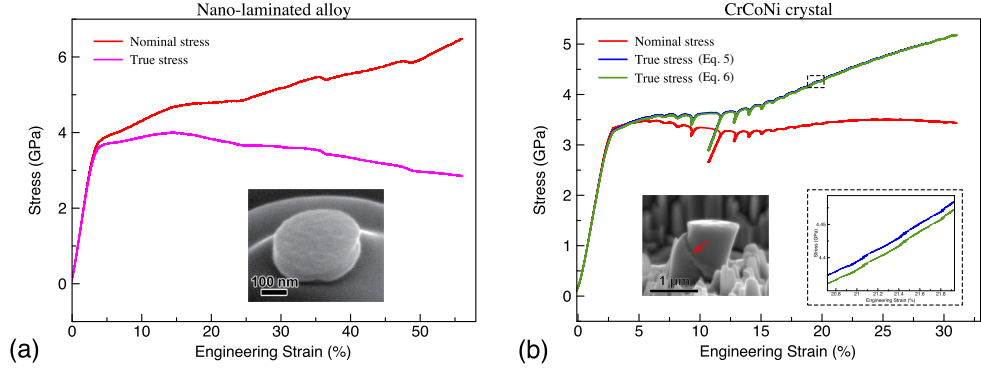


Fig. 5 Engineering strain vs. nominal stress (red) and true stress (blue) curves. Nominal stress values are taken from Wu et al (2021)) and the calculated true stress curves are calculated using the formulas derived here. (a) homogeneous deformation of a crystal-glass nano-laminated alloy sample calculated with the classical formulas (1), (2); (b) single shear band deformation of a CrCoNi crystal calculated with formulas (1), (5) (blue) and simplified formula (6) (green). Insets show the final state of the pillar at the end of the loading.

As an example, we will reconsider the strain-stress behavior of a crystal-glass symbiotic alloy investigated in Wu et al (2021). In this study, the authors plotted the engineering strain-stress curves to characterize the crystal-glass nano-laminated alloy sample’s mechanical properties compared with its crystalline and amorphous counterparts. Interestingly, the authors found that the nano-laminated crystal-glass alloy appeared to be tougher than its individual components when analyzing the engineering stress data (see Fig. 4(a) in Wu et al (2021)). However, when we calculate the engineering strain vs. true stress curves for two cases: (i) the crystal-glass nano-laminated alloy undergoing homogeneous deformation using the conventional formula provided in (2); (ii) the CrCoNi crystal experiencing slip band deformation using (5) with $\alpha = \pi/4$, $f_0 = 1$, $\epsilon_e = 2.5\%$ and $\sigma_e^{eng} = 3.23$ GPa (or the simplified formula given in (6)), we observe a contradictory outcome in both cases. Specifically, the nano-laminated alloy exhibits softening, as shown in Fig. 5(a), while the CrCoNi crystal demonstrates hardening, as depicted in Fig. 5(b). This finding emphasizes the significance of taking into account the current deformation state of the material, even in the absence of a strong localization.

We have to notice that, for the nano-laminated crystal-glass alloy, we deal with a bulging deformation, and one could expect that the true stress obtained through (2) is slightly underestimated. Indeed, from the final shape of the pillar, we observe that the central radius R_m is less than 3% of the volume-preserving radius R , hence the underestimation of true stress is less than 6% at the end of the deformation. This is negligible with respect to the difference between engineering and true stress, plotted in Fig. 5(a), which is on the order of 100%, and cannot change the above conclusions.

Lastly, we emphasize that when comparing the true stress curves obtained using (5) and the simplified formulas provided in (6), as shown in Fig. 5(b), we observed minimal differences, even at high strains.

5 Conclusion

In conclusion, our study provides formulas for calculating true stress in cases where slip/kink bands form during mechanical loading in compression experiments on pillars. These formulas are simple and need only the engineering stress data, some geometric data (aspect ratio), and some mechanical data (elastic limit) which are easy to get from the experimental results. For slip/kink band plastic deformation the shear stress τ acting in the band can be recovered from the uniaxial true stress σ^{true} . The diagram shear plastic strain- shear stress is then the main information on the mechanical behavior of the material that can be obtained from a pillar experiment with a shear band localization.

Of course, our formula does not consider bending and torsion, which cannot be easily traced by simple geometrical arguments. However, in our opinion, their effects will be of second-order. In a 2D finite element numerical simulation of Eulerian elasto-plastic pillar compression, we compared the formula-based true stress with the theoretical true stress and we found a good agreement.

A more precise alternative to these simple formulas could be very long and difficult FE computations involving large deformations. Moreover, the FE computations need to know in advance the material type (mono-crystal, poly-crystal, isotropic), its behavior (hardening, softening, etc) and the constants that characterize the material. This means that when localization occurs, the proposed geometric formula gives the possibility to experimenters to interpret the data in a simple manner without any preconceived notions about the choice of model.

However, using these formulas, we re-evaluated the robustness of previous experimental results and found that considering the current deformation state of engineered materials can be important for accurately interpreting their mechanical behavior at small scales. To be more precise, our analysis revealed that, in some cases, the true stress led to conclusions that were exactly opposite to those found using the engineering stress, while in other cases, the difference is mainly quantitative and the overall trend is similar. To conclude, our work provides a valuable tool for accurately interpreting the mechanical behavior of materials under compressive loads and for drawing appropriate conclusions based on the true stress values.

Acknowledgments. O.U.S. is supported by the grants ANR-18-CE42-0017-03, ANR-19-CE08-0010-01, ANR-20-CE91-0010, M.G. is supported by the grant ANR-21-CE08-0003-01 and I.I. acknowledges the support of the Romanian Ministry of Research (PN-III-P4-PCE-2021-0921 within PNCDI III).

Declarations

The authors disclose any interests that are directly or indirectly related to the present paper. It has obtained approval for publication from all co-authors and does not involve any human or animals participants.

References

- Basak AK, Pramanik A, Prakash C (2019) Deformation and strengthening of SiC reinforced Al-MMCs during in-situ micro-pillar compression. *Materials Science and Engineering: A* 763:138141
- Belytschko T, Liu WK, Moran B, et al (2014) *Nonlinear Finite Element for Continua and Structures*. John Wiley and Sons, Chichester, UK
- Chen M, Pethö L, Sologubenko AS, et al (2020) Achieving micron-scale plasticity and theoretical strength in silicon. *Nat Commun* 11(1):2681
- Cui Y, Aydogan E, Gigax JG, et al (2021) In situ Micro-Pillar compression to examine Radiation-Induced hardening mechanisms of FeCrAl alloys. *Acta Mater* 202:255–265
- Frick CP, Clark BG, Orso S, et al (2008) Size effect on strength and strain hardening of small-scale [111] nickel compression pillars. *Materials Science and Engineering: A* 489(1):319–329
- Friedman N, Jennings AT, Tsekenis G, et al (2012) Statistics of dislocation slip avalanches in nanosized single crystals show tuned critical behavior predicted by a simple mean field model. *Phys Rev Lett* 109(9):095507
- Gan K, Zhu S, Jiang S, et al (2020) Study on stochastic nature of plasticity of Cu/Zr metallic glass micropillars. *J Alloys Compd* 831:154719
- Ghidelli M, Orekhov A, Bassi AL, et al (2021) Novel class of nanostructured metallic glass films with superior and tunable mechanical properties. *Acta Mater* 213:116955
- Greer JR, Oliver WC, Nix WD (2005) Size dependence of mechanical properties of gold at the micron scale in the absence of strain gradients. *Acta Mater* 53(6):1821–1830
- Hagihara K, Mayama T, Honnami M, et al (2016) Orientation dependence of the deformation kink band formation behavior in zn single crystal. *Int J Plast* 77:174–191
- Han Z, Yang H, Wu WF, et al (2008) Invariant critical stress for shear banding in a bulk metallic glass. *Appl Phys Lett* 93(23):231912
- Inamura T (2019) Geometry of kink microstructure analysed by rank-1 connection. *Acta Mater* 173:270–280
- Kiener D, Guruprasad PJ, Keralavarma SM, et al (2011) Work hardening in micropillar compression: In situ experiments and modeling. *Acta Mater* 59(10):3825–3840
- Lee SW, Han SM, Nix WD (2009) Uniaxial compression of fcc au nanopillars on an MgO substrate: The effects of prestraining and annealing. *Acta Mater* 57(15):4404–4415

- Maaß R, Meza L, Gan B, et al (2012) Ultrahigh strength of dislocation-free Ni₃Al nanocubes. *Small* 8(12):1869–1875
- Marano A, Gélébart L, Forest S (2021) FFT-based simulations of slip and kink bands formation in 3D polycrystals: Influence of strain gradient crystal plasticity. *J Mech Phys Solids* 149:104295
- Mayer CR, Yang LW, Singh SS, et al (2016) Anisotropy, size, and aspect ratio effects on micropillar compression of AlSiC nanolaminate composites. *Acta Mater* 114:25–32
- Nandam SH, Schwaiger R, Kobler A, et al (2021) Controlling shear band instability by nanoscale heterogeneities in metallic nanoglasses. *J Mater Res* 36(14):2903–2914
- Ng KS, Ngan AHW (2008) Stochastic nature of plasticity of aluminum micro-pillars. *Acta Mater* 56(8):1712–1720
- Nizolek TJ, Pollock TM, McMeeking RM (2021) Kink band and shear band localization in anisotropic perfectly plastic solids. *J Mech Phys Solids* 146:104183
- Rizzardi Q, Derlet PM, Maaß R (2022) Intermittent microplasticity in the presence of a complex microstructure. *Phys Rev Mater* 6(7):073602
- Salman OU, Ionescu IR (2021) Tempering the mechanical response of FCC micropillars: An eulerian plasticity approach. *Mech Res Commun* 114(103665):103665
- Salman OU, Baggio R, Bacroix B, et al (2021) Discontinuous yielding of pristine micro-crystals. *C R Phys* 22(S3):1–48
- Uchic MD, Dimiduk DM, Florando JN, et al (2004) Sample dimensions influence strength and crystal plasticity. *Science* 305(5686):986–989
- Wang JG, Hu YC, Guan PF, et al (2017) Hardening of shear band in metallic glass. *Sci Rep* 7(1):7076
- Wang ZJ, Shan ZW, Li J, et al (2012) Pristine-to-pristine regime of plastic deformation in submicron-sized single crystal gold particles. *Acta Mater* 60(3):1368–1377
- Weiss J, Zhang P, Salman OU, et al (2021) Fluctuations in crystalline plasticity. *C R Phys* 22(S3):1–37
- Wu G, Liu C, Brognara A, et al (2021) Symbiotic crystal-glass alloys via dynamic chemical partitioning. *Mater Today* 51:6–14
- Zhang J, Kishida K, Inui H (2017a) Specimen size and shape dependent yield strength in micropillar compression deformation of mo single crystals. *Int J Plast* 92:45–56
- Zhang P, Salman OU, Zhang JY, et al (2017b) Taming intermittent plasticity at small scales. *Acta Mater* 128:351–364

Zhang P, Salman OU, Weiss J, et al (2020) Variety of scaling behaviors in nanocrystalline plasticity. *Phys Rev E* 102(2-1):023006

Zhang Y, Li N, Schneider MM, et al (2022) Kink mechanism in Cu/Nb nanolaminates explored by in situ pillar compression. *Acta Mater* 237:118150

6 Annex: Elastic perfectly plastic Eulerian model

The movement (flow) in the Eulerian description is given by the velocity field, denoted $\mathbf{v}(t, \cdot) : \mathcal{D}_t \rightarrow \mathbb{R}^d$ (here \mathcal{D}_t is the Eulerian domain occupied by the elasto-plastic body at time t). The rate of deformation and the spin rate are denoted by $\mathbf{D} = \mathbf{D}(\mathbf{v}) = (\nabla \mathbf{v} + \nabla^T \mathbf{v})/2$ and by $\mathbf{W} = \mathbf{W}(\mathbf{v}) = (\nabla \mathbf{v} - \nabla^T \mathbf{v})/2$, respectively while the Cauchy stress tensor is $\boldsymbol{\sigma}(t, \cdot) : \mathcal{D}_t \rightarrow \mathbb{R}_S^{d \times d}$. To describe the elasto-plastic Eulerian model (see for instance [Belytschko et al \(2014\)](#)), we consider the additive decomposition of the rate deformation tensor into the elastic \mathbf{D}^e and plastic rates \mathbf{D}^p of deformation

$$\mathbf{D} = \mathbf{D}^e + \mathbf{D}^p.$$

For the elastic range we considered the generalization of Hooke's law written in terms of the Jaumann rate of the Cauchy stress tensor $\boldsymbol{\sigma}^\nabla = \dot{\boldsymbol{\sigma}} - \mathbf{W}\boldsymbol{\sigma} - \boldsymbol{\sigma}\mathbf{W}$ (here $\dot{\boldsymbol{\sigma}} = \partial_t \boldsymbol{\sigma} + \mathbf{v} \cdot \nabla \boldsymbol{\sigma}$ is the total derivative) given by

$$\boldsymbol{\sigma}^\nabla(t) = \lambda \text{trace}(\mathbf{D}^e) \mathbf{I} + 2\mu \mathbf{D}^e, \quad \text{in } \mathcal{D}_t,$$

where λ, μ are the Lamé elastic coefficients. The plastic rate of deformation is related to the Cauchy stress tensor through the flow rule associated to the classical Von-Mises yield criterion with no hardening (perfectly plastic material). To be more precise, let $\mathcal{F}(\boldsymbol{\sigma}) = \sigma_{eq} - \sigma_Y$ be the yield function, with σ_Y the yield limit and $\sigma_{eq} = \sqrt{\frac{3}{2}} |\boldsymbol{\sigma}^D|$ the Von-Mises stress ($\boldsymbol{\sigma}^D = \boldsymbol{\sigma} - \frac{1}{3} \text{trace}(\boldsymbol{\sigma}) \mathbf{I}$ is the stress deviator). If we denote the accumulated plastic strain by ε^p (given through the differential equation $\dot{\varepsilon}^p = \sqrt{\frac{3}{2}} |\mathbf{D}^p|$), then the flow rule and the loading-unloading conditions read

$$\mathbf{D}^p = \frac{\dot{\varepsilon}^p}{\sigma_{eq}} \boldsymbol{\sigma}^D, \quad \dot{\varepsilon}^p \geq 0, \quad \mathcal{F}(\boldsymbol{\sigma}) \leq 0, \quad \dot{\varepsilon}^p \mathcal{F}(\boldsymbol{\sigma}) = 0.$$